Seismic-generated unsteady motions in shallow basins and channels. Part II: Numerical modelling

Seismic-generated unsteady motions in shallow basins and channels. Part II: Numerical modelling

Andrea Maranzoni*, Paolo Mignosa

University of Parma
Department of Engineering and Architecture
Parco Area delle Scienze, 181/A
43124 Parma, Italy

* Corresponding author, e-mail: andrea.maranzoni@unipr.it

Abstract In this paper unsteady motions generated by seismic-type excitation are simulated by a 2D depth-averaged mathematical model based on the classic shallow water approximation. A suitable time-dependent forcing term is added in the governing equations, and these are solved by a MUSCL-type shock-capturing finite volume scheme with a splitting treatment of the source term. The HLL approximate Riemann solver is used to estimate the numerical fluxes. The accuracy of the numerical scheme is assessed by comparison with novel exact solutions of test cases concerning sinusoidally-generated sloshing in a prismatic tank, a rectangular open channel, and a parabolic basin. A sensitivity analysis is performed on the influence of the relevant dimensionless parameters. Moreover, numerical results are validated against experimental data available in literature concerning shallow water sloshing in a swaying tank. Finally, real-scale applications to a reservoir created by a dam and an urban water-supply storage tank are presented. The results show that the model provides accurate solutions of the shallow water equations with a seismic-type source term and can be effectively adopted to predict the main flow features of the unsteady motion induced by horizontal seismic acceleration when the long wave assumption is valid.

Highlights

- Seismic-generated unsteady motions are modelled by the 2D depth-averaged shallow water equations.
- The numerical solution is obtained by a Godunov-type shock-capturing finite volume scheme.
- Numerical tests of sloshing motion are carried out and numerical results are compared with analytical solutions.
- A sensitivity analysis is performed on the influential parameters.
- The numerical model is validated against experimental data and two examples of field-scale applications to real reservoirs are presented.

Keywords Seismic-induced water motion; 2D shallow water equations; Numerical modelling; Finite volume method; Sensitivity analysis; Real-field applications.

1. Introduction

The generation of water waves on free surface bodies is one of the damaging effects of earthquakes. In a lake formed by a dam, for instance, waves caused by seismic excitation may generate a run-up on the upstream face of the dam in the order of the freeboard available, thereby leading to the potential risk of dam overtopping [1,2]. Such an event may have serious consequences, including structural damages to the crest and downstream face of the dam (especially for embankment dams), and to power plants or other features located in the downstream area near the dam's toe [3]. Hazards to the operating personnel cannot be ruled out either. Hence, national technical guidelines on dam safety and protection commonly prescribe freeboard requirements in order to provide for a reassuring safety margin against wave-induced dam overtopping, even during seismic events (e.g. [1,4,5]). The occurrence of seismic seiches in free surface water bodies, such as lakes, ponds, reservoirs, sewage or water supply storages, basins formed by dams, or even swimming pools, is actually documented in literature with reference to a number of strong historical earthquakes (see [6–8]). For example, remarkable seiches were observed in several lakes, rivers, and bays during the 1755 Lisbon earthquake, the 1950 Assam earthquake, and the 1964 Alaskan earthquake, even at a great distance from the epicentre [6,9]. More recently, according to Barberopoulou et al. [10], the 2002 Alaskan Denali earthquake triggered notable seiches as far away as British Columbia and Washington State. As regards dam reservoirs, Scawthorn [11] reports that during the Marmara earthquake on August 17, 1999, a seiche of 2 m amplitude was experienced in the lake created by the Yuvacik dam (western Turkey), and dam overtopping was prevented because the basin was not full at the time of the earthquake [2]. Hinks and Gosschalk [12] report the testimony of an eyewitness who observed the dynamics of the seismic seiches generated by the Yellowstone earthquake on August 17, 1959, in the lake formed by the Hebgen embankment dam (Montana, USA). During this seismic event, which occurred when the Lake Hebgen was full, the water flowed over the dam four times, and a maximum head of 1 m above the dam crest was estimated. Seismic-generated water oscillations generally also induce water run-up on the sloping edges of the reservoir and an increase in the pressure load on the retaining structures compared to the undisturbed stationary condition. In open channels, earthquakes may generate anomalous waves, with consequent risk of bank overtopping.

In general, the analysis of the seismic response of a confined free surface body is very important in many

engineering problems, in order to prevent spillage or damages to retaining systems. Accordingly, the problem of liquid oscillations in a horizontally accelerated tank has gained great attention in the past few decades, and theoretical investigations have been carried out based on the assumption of small-amplitude waves (e.g. [13–16]) or finite-amplitude waves (e.g. [17–21]). In the latter case, depth-averaged flow equations can be used if the long-wave hypothesis is allowable. In this framework, Boussinesq-type models, accounting for a non-hydrostatic pressure distribution, are suitable to describe free surface flows when the vertical acceleration is not negligible (e.g. [22–28]). On the contrary, when the vertical acceleration can be disregarded, the classic shallow water approximation can be adopted, based on the assumption of hydrostatic pressure distribution. This approach is commonly used in engineering practice in various free surface flow applications, mainly concerning flood routing in open channels (e.g. [29–32]), and dam-break and flood inundation modelling (e.g. [33–39]).

A two-dimensional (2D) hydrostatic depth-averaged shallow water model is used in this paper to simulate seismic-generated unsteady motions in reservoirs and open channels. To this purpose a specific time-dependent source term is added to the governing equations in order to include the horizontal oscillating forcing effect due to an essentially undulatory earthquake. The 2D shallow water equations (SWE) are numerically solved using a second-order accurate shock-capturing Godunov-type finite volume scheme, coupled with a splitting decomposition of the source term. Boundary-extrapolated values are reconstructed by means of the classic MUSCL-Hancock scheme [40,41] according to the Weighted Surface-Depth Gradient Method (WSDGM) proposed by Aureli et al. [35], and numerical fluxes are computed using the HLL (Harten, Lax and van Leer) approximate Riemann solver [40,42].

Model accuracy is assessed on the basis of numerical tests concerning sloshing waves induced by sinusoidal time-varying horizontal acceleration on a water body initially at rest contained in a prismatic rectangular tank or a parabolic basin, and on a uniform flow taking place in a rectangular open channel. Numerical results are compared with the analytical solutions presented by Maranzoni and Mignosa [43] in Part I of this work. In particular, the test concerning sloshing in a parabolic basin is characterized by the presence of a moving shoreline, thus the numerical model must be able to accomplish a robust treatment of wetting and drying fronts [35]. A sensitivity analysis on the parameters characterizing the forcing excitation is performed to assess their influence on the flow dynamics and, especially, on the maximum free surface displacement. The model is then validated against experimental data available in literature concerning shallow water sloshing induced by a sway motion in a rectangular tank [21]. Finally, unsteady motions induced by a seismic-type loading in both a real lake created by a dam and a real water-supply storage tank are simulated to test the capabilities of the

numerical model in field-scale applications. In the former application, the cases of both sinusoidal and real seismic horizontal acceleration are considered.

The paper is organized as follows. Section 2 is devoted to the description of the mathematical model and the numerical scheme used to solve the governing equations. The numerical results are compared with analytical solutions in Section 3. Validation of the model against experimental data available in literature is performed in Section 4, and two real-field applications are presented in Section 5. Conclusions are drawn in Section 6.

2. Numerical model

The 2D depth-averaged SWEs are suitable to model finite-amplitude long waves in shallow water and, in the vector conservation form, read (e.g. [40,41]):

$$\frac{\partial \mathbf{U}}{\partial t}+\frac{\partial \mathbf{F}}{\partial x}+\frac{\partial \mathbf{G}}{\partial y}=\mathbf{S}\,, \tag{1}$$

where **U** is the vector of the conserved variables, **F** and **G** are the vectors of the physical fluxes along the horizontal x and y directions, respectively, **S** is the source term vector, and t is time. In a non-inertial frame of reference linearly accelerating relative to a stationary inertial one, it is [43]:

$$\mathbf{U}=\begin{bmatrix} h \\ uh \\ vh \end{bmatrix},\quad \mathbf{F}=\begin{bmatrix} uh \\ u^2h+\frac{1}{2}gh^2 \\ uvh \end{bmatrix},\quad \mathbf{G}=\begin{bmatrix} vh \\ uvh \\ v^2h+\frac{1}{2}gh^2 \end{bmatrix},\quad \mathbf{S}=\begin{bmatrix} 0 \\ gh(S_{0x}-S_{\mathrm{f}x})+a_xh \\ gh(S_{0y}-S_{\mathrm{f}y})+a_yh \end{bmatrix}, \tag{2}$$

in which h is the water depth, u and v are the horizontal velocity components relative to the ground along the x and y axes, respectively, S_{0x} and S_{0y} are the bottom slopes in the x and y directions (i.e. $S_{0x}=-\partial z_\mathrm{b}/\partial x$ and $S_{0y}=-\partial z_\mathrm{b}/\partial y$, z_b being the bottom elevation above a datum), $S_{\mathrm{f}x}$ and $S_{\mathrm{f}y}$ are the friction slopes along the same directions, g is the acceleration due to gravity, and a_x and a_y are the x- and y-components of the apparent rectilinear acceleration in the non-inertial reference frame. The additional source terms in Eq. (2) are suitable to represent the forcing effect of a horizontal seismic excitation on a water body in the reference frame moving with the shaking ground, if accelerograms representative of the time variation of the ground acceleration during an earthquake are used. Real seismic accelerograms are usually provided as time series. However, unidirectional harmonic forcing excitation is often considered as a first approximation in earthquake engineering (e.g. [14]). In this case, a_x and a_y are assumed to vary sinusoidally in time, as

$$a_x=\begin{cases} A_x\sin(\omega t) & \text{if } 0\le t\le D \\ 0 & \text{if } t>D \end{cases}\quad\text{and}\quad a_y=\begin{cases} A_y\sin(\omega t) & \text{if } 0\le t\le D \\ 0 & \text{if } t>D \end{cases}\,, \tag{3}$$

in which A_x and A_y are the amplitudes of the periodic acceleration in the x and y directions, respectively, ω is the

angular frequency of the oscillation, and D is the duration of the forcing excitation (which for simplicity is hypothesized equal to a multiple of the forcing period $2\pi/\omega$ in this paper). The frictional terms are expressed through the classic Manning formula:

$$S_{\mathrm{fx}} = \frac{n^2 u\sqrt{u^2+v^2}}{h^{4/3}}, \quad S_{\mathrm{fy}} = \frac{n^2 v\sqrt{u^2+v^2}}{h^{4/3}}, \tag{4}$$

n being the Manning roughness coefficient.

The dimensional analysis performed by Maranzoni and Mignosa [43] has shown that if unidirectional harmonic forcing is considered, the dimensionless parameters involved in the problem are the twin ratios $A_x L/(gh_0)$ and $A_y L/(gh_0)$, and the group $\omega L(gh_0)^{-1/2}$, where h_0 is a characteristic water height and L a typical horizontal length scale of the flow field along the direction of the excitation. The first two groups are forcing parameters (denoted hereinafter as F_x and F_y, respectively) representing in dimensionless form the amplitude of the exciting acceleration components in the x and y directions, respectively, whereas the last group represents the Strouhal number (denoted by St hereinafter).

Eq. (1) is solved numerically on a Cartesian grid by an explicit MUSCL-Hancock, Godunov-type finite volume scheme based on a second-order accurate Strang splitting decomposition of the source term [42]. For each cell (i,j), the current cell-average state $\mathbf{U}_{i,j}^{n}$ at time level t^n is updated to the new flow state $\mathbf{U}_{i,j}^{n+1}$ at time t^{n+1} by the computational time step $\Delta t = t^{n+1} - t^n$ through the following three-step algorithm:

$$\begin{aligned}
\mathbf{U}_{i,j}^{*} &= \mathbf{U}_{i,j}^{n} + \frac{\Delta t}{2}\mathbf{S}_{i,j}^{n} \\
\mathbf{U}_{i,j}^{**} &= \mathbf{U}_{i,j}^{*} - \frac{\Delta t}{\Delta x}\left[\mathbf{F}_{i+1/2,j} - \mathbf{F}_{i-1/2,j}\right] - \frac{\Delta t}{\Delta y}\left[\mathbf{G}_{i,j+1/2} - \mathbf{G}_{i,j-1/2}\right] \\
\mathbf{U}_{i,j}^{n+1} &= \mathbf{U}_{i,j}^{**} + \frac{\Delta t}{2}\mathbf{S}_{i,j}^{**},
\end{aligned} \tag{5}$$

in which $\mathbf{U}_{i,j}^{*}$ and $\mathbf{U}_{i,j}^{**}$ are two successive intermediate updates of $\mathbf{U}_{i,j}$; $\mathbf{F}_{i\pm1/2,j}$ and $\mathbf{G}_{i,j\pm1/2}$ are the numerical fluxes in the x and y directions, respectively, and $\mathbf{S}_{i,j}$ is the cell-averaged source term. A pointwise discretization of the source term is performed in Eq. (5), and numerical fluxes are assessed in the advection step (based on intermediate update $\mathbf{U}^{*}$) by using the MUSCL-Hancock scheme coupled with the HLL approximate Riemann solver. According to the HLL approach, the $\mathbf{F}_{i+1/2,j}$ flux is given by [40,42]

$$\mathbf{F}_{i+1/2,j} = \begin{cases} \mathbf{F}_{\mathrm{L}} & \text{if } c_{\mathrm{L}} \geq 0 \\ \dfrac{c_{\mathrm{R}}\mathbf{F}_{\mathrm{L}} - c_{\mathrm{L}}\mathbf{F}_{\mathrm{R}} + c_{\mathrm{L}}c_{\mathrm{R}}(\mathbf{U}_{\mathrm{R}} - \mathbf{U}_{\mathrm{L}})}{c_{\mathrm{R}} - c_{\mathrm{L}}} & \text{if } c_{\mathrm{L}} \leq 0 \leq c_{\mathrm{R}} \\ \mathbf{F}_{\mathrm{R}} & \text{if } c_{\mathrm{R}} \leq 0 \end{cases}, \tag{6}$$

in which $\mathbf{U}_L$ and $\mathbf{U}_R$ are the vectors of the evolved boundary-extrapolated conserved variables on the left- and right-hand sides of the cell boundary, respectively; correspondingly, $\mathbf{F}_L$ and $\mathbf{F}_R$ are the vectors of physical fluxes calculated for $\mathbf{U}_L$ and $\mathbf{U}_R$, and c_L and c_R are suitable estimates of the left and right wave celerities [40]. The boundary-extrapolated variables are computed via a piecewise linear reconstruction based on the Weighted Surface-Depth Gradient Method (WSDGM) proposed by Aureli et al. [35], and the Van Leer slope limiter function [40,41] is applied to avoid spurious oscillations. A schematic of the linear extrapolation of interface values (along the x-axis direction) and HLL approximate Riemann solver for $c_L \leq 0 \leq c_R$ is reported in Fig. 1. The mass-conserving flux correction technique proposed by Aureli et al. [35] is used at wetting and drying fronts. This special treatment, based on the introduction of a wet/dry threshold water depth, allows effective handling of the well-known numerical difficulties which arise near moving fronts [44,45]. For more detail about the numerical algorithm, see Aureli et al. [35].

Due to the explicit character of the algorithm, the computational time step must be set so as to satisfy a suitable stability condition which, for unsplit 2D schemes, can be adapted as [42,46]

$$\Delta t = \frac{\mathrm{Cr}}{2} \min\left(\min_{i,j} \frac{\Delta x}{|u_{i,j}| + \sqrt{g h_{i,j}}}, \min_{i,j} \frac{\Delta y}{|v_{i,j}| + \sqrt{g h_{i,j}}} \right), \tag{7}$$

where Cr (≤ 1) denotes the Courant number coefficient. However, the time step used to advance the numerical solution in time should also guarantee accurate discretization of the time-dependent forcing source term. To fulfil this requirement and prevent aliasing problems, the computational "sampling" frequency $1/\Delta t$ must be at least two (and preferably more) times the highest frequency of the time-varying forcing waveform, according to the Nyquist sampling criterion (e.g. [47]). Accordingly, the Nyquist number Nq of the computations, defined as the ratio of the sampling frequency to the forcing frequency [i.e. $\mathrm{Nq} = 2\pi/(\omega\, \Delta t)$], must be greater than 2 at each time step. In this work, it is assumed that a sufficiently accurate reproduction of the time-dependent forcing acceleration is ensured if $\mathrm{Nq} \geq 20$. In the cases in which this antialiasing condition is expected to be more restrictive than the stability condition, the calculations are performed by suitably reducing the value of the Courant number coefficient.

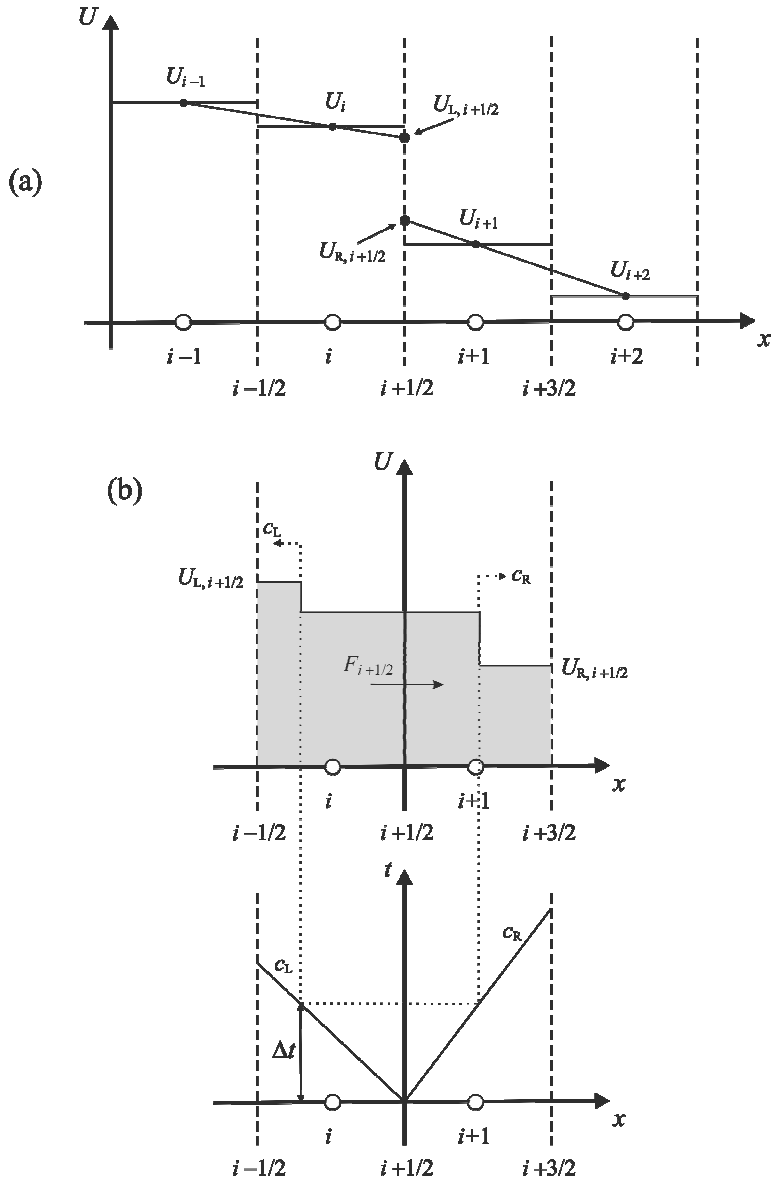

Fig. 1. Sketch of the linear extrapolation of interface variables along the x-axis direction (a) and structure of the Riemann problem solution at $(i + 1/2,j)$-intercell boundary for $c_L \le 0 \le c_R$ according to the HLL approximate Riemann solver (b).

3. Numerical tests

In order to assess model accuracy some numerical tests concerning sloshing motions in systems subject to sinusoidal time-varying horizontal acceleration are performed in this section. The numerical results are compared with the analytical solutions obtained by Maranzoni and Mignosa [43] in Part I of this work.

3.1. Seismic water waves in a prismatic tank

The first numerical test concerns the frictionless sloshing induced by an earthquake on a water mass stored in a prismatic tank with a horizontal square bottom of size $L = 10$ m and lateral vertical sides normal to the

reference axes x and y (Fig. 1). The tank is initially filled with water at rest of height $h_0 = 1$ m, and horizontal x-acceleration varying sinusoidally in time is applied for a fixed duration D. The solid walls are assumed to be high enough to avoid overflow.

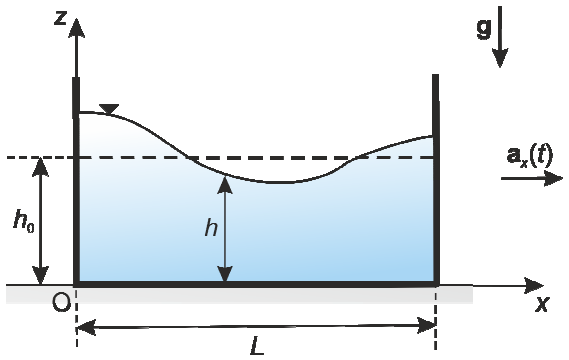

Fig. 2. Definition sketch for the problem of seismic-generated oscillations in a prismatic tank (Oxz is a linearly-accelerating non-inertial frame of reference, with the origin located at the left-hand lower corner of the tank).

Two forcing excitations having the same frequency $\omega = 2\pi$ rad/s (St $\cong$ 20) are considered: the former is characterized by $A_x = 0.1g$, whereas the latter by $A_x = 0.5g$ (corresponding to $F_x = 1$ and $F_x = 5$, respectively). These two situations are very different, but realistic: no surge develops in the former case, whereas in the latter the steepening of the wave front of smooth positive waves is expected to cause the formation of bores [43]. The numerical simulations are performed by discretizing the computational domain with square cells sized $\Delta x = \Delta y = 0.05$ m. The Courant number coefficient is set at 0.9, which guarantees that the Nyquist number of the computations is in the order of 10^2.

Figs. 3 and 4 compare analytical and numerical water depth and velocity profiles at selected times for the two cases considered. For the excitation characterized by $A_x = 0.5g$ and $\omega = 2\pi$ rad/s (Fig. 4), the comparison is performed for time $t = 0.69$ s, when the positive wave originated at the right-hand side wall of the tank becomes a surge. Figs. 3 and 4 show that numerical results agree very well with the analytical solution. In particular, the numerical model correctly reproduces both the negative and positive waves originated at the end walls, and accurately predicts the intermediate flow state between the two waves. Due to its simplicity (see [48]) and its suitability in conservation law problems [41], the classic mean absolute error (MAE) is used here to provide a synthetic global quantification of the model's accuracy in predicting water depth and velocity profiles at a selected time. The numerical water depth and velocity profiles reported in Fig. 3 approximate the exact solutions obtained by the method of characteristics with mean absolute errors of $2.2 \cdot 10^{-4}$ m and $6.8 \cdot 10^{-4}$ m/s,

respectively. As regard the profiles of Fig. 4, MAE is equal to $1.7 \cdot 10^{-3}$ m for the water depth profile, and to $5.5 \cdot 10^{-3}$ m/s for the velocity profile.

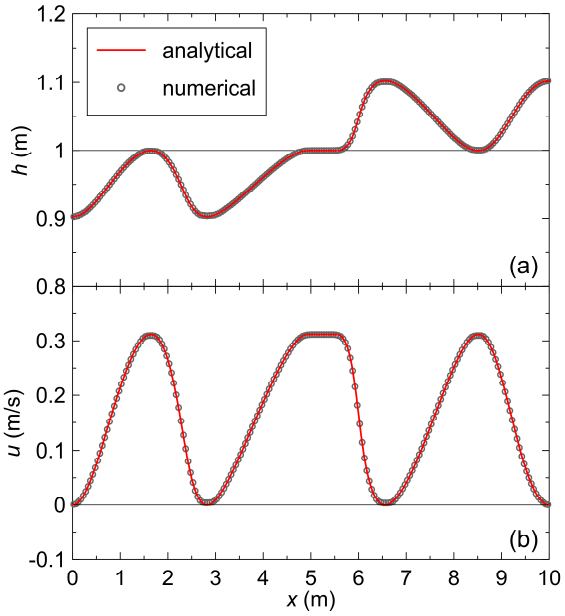

Fig. 3. Sinusoidally-forced oscillations in a prismatic tank ($L = 10$ m, $h_0 = 1$ m, $A_x = 0.1g$, $\omega = 2\pi$ rad/s): comparison between analytical and numerical water surface (a) and velocity (b) profiles at $t = 1.5$ s ($\Delta x = \Delta y = 0.05$ m).

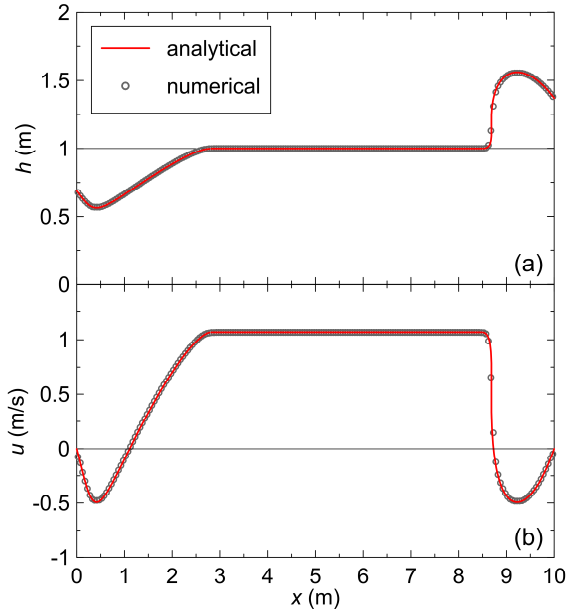

Fig. 4. Sinusoidally-forced oscillations in a prismatic tank ($L = 10$ m, $h_0 = 1$ m, $A_x = 0.5g$, $\omega = 2\pi$ rad/s): comparison between analytical and numerical water surface (a) and velocity (b) profiles at $t = 0.69$ s ($\Delta x = \Delta y = 0.05$ m).

Again with reference to the test case with $A_x = 0.5g$ and $\omega = 2\pi$ rad/s, Fig. 5 shows the computed water depth and velocity time series at the middle section of the tank ($x = L/2$). The theoretical solution obtained by Maranzoni and Mignosa [43] for $0 \leq t \leq t_M$ is also reported for comparison, where $t_M \cong 1.31$ s is the time at which the negative wave coming from the left-hand side wall of the tank reaches the middle section. Similarly, Fig. 6 shows the time histories of the water depth at the two side walls; the exact solution is represented in the interval [0, $t_G \cong 1.62$ s] for $x = 0$, and [0, $t_F \cong 1.10$ s] for $x = L$ [43]. During the first stages of the sloshing motion, at $x = L/2$ the water surface remains undisturbed until the arrival (at $t = t_M$) of the negative wave originated at the left end wall (Fig. 5a), whereas the water velocity varies sinusoidally with time due to the sinusoidal acceleration transmitted to the water volume by the earthquake (Fig. 5b). At the end walls (Fig. 6), the water level varies sinusoidally, showing a negative variation with reference to the initial still-water level at $x = 0$, and a positive variation at $x = L$. After a few instants, the time series of Figs. 5 and 6 show a complex oscillating pattern caused by several wave interactions and the possible development of bores, and the oscillations of the flow variables appear quite asymmetric with reference to the initial undisturbed values. The frequency of the sloshing motion decreases sensibly once the seismic disturbance has ended. However, significant variations in water depth continue to occur in this transient free-oscillating phase, even if the excursion between positive and negative extrema diminishes compared to the excitation phase. It is worth noting that the predicted and analytical time series shown in Figs. 5 and 6 can be compared only in a limited time range, since the analytical solutions derived by Maranzoni and Mignosa [43] using the method of characteristics are limited to the first stages of the sinusoidally-forced sloshing and concern smooth waves only.

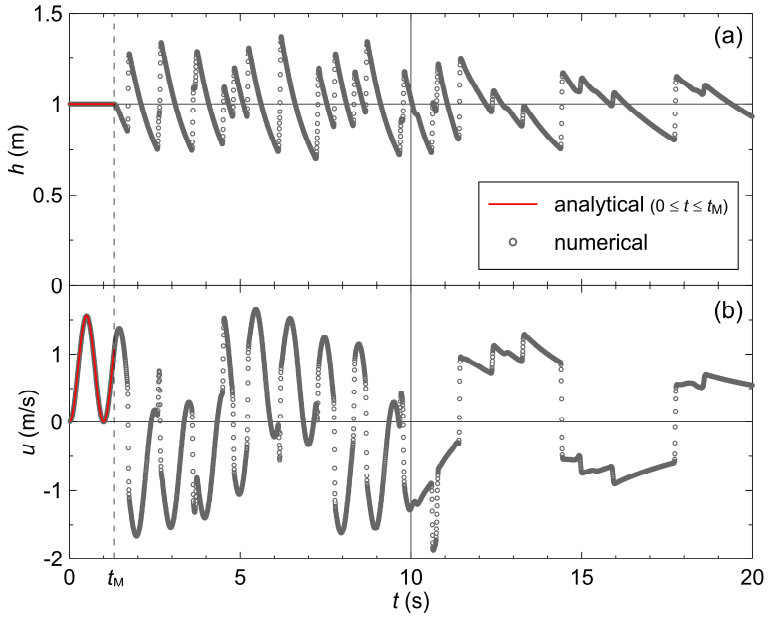

Fig. 5. Sinusoidally-forced oscillations in a prismatic tank (L = 10 m, h_0 = 1 m, $A_x = 0.5g$, $\omega = 2\pi$ rad/s, D = 10 s): time series of computed water height (a) and velocity (b) at $x = L/2$ ($\Delta x = \Delta y$ =0.05 m). The analytical solution is reported for $0 \le t \le t_M$ ($t_M \cong 1.31$ s).

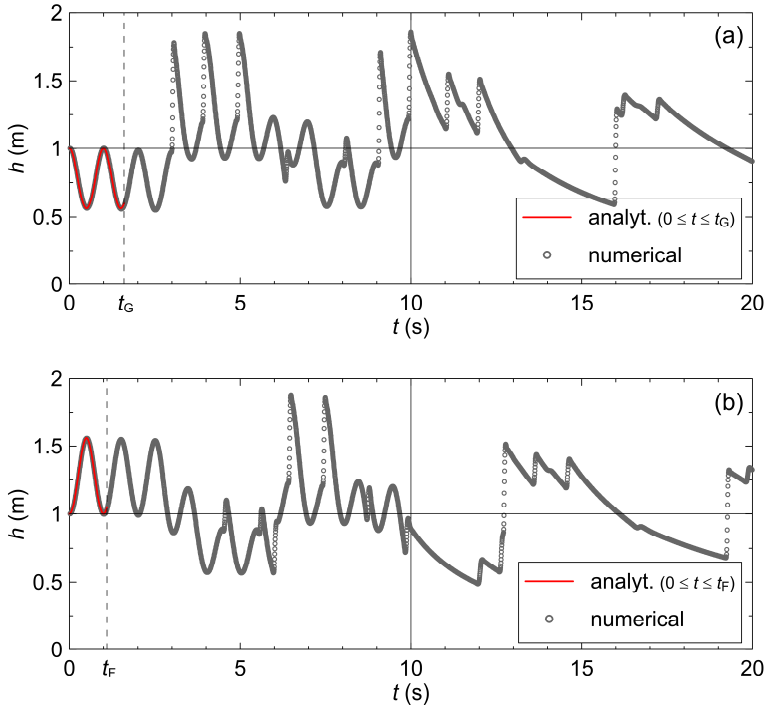

Fig. 6. Sinusoidally-forced oscillations in a prismatic tank (L = 10 m, h_0 = 1 m, $A_x = 0.5g$, $\omega = 2\pi$ rad/s, D = 10 s): time series of computed water height at $x = 0$ (a) and $x = L$ (b) ($\Delta x = \Delta y$ =0.05 m). The analytical solutions are reported for $0 \le t \le t_G$ ($t_G \cong 1.62$ s) and $0 \le t \le t_F$ ($t_F \cong 1.10$ s), respectively.

The response of the system in Fig. 2 to a seismic-type disturbance is further characterized by a sensitivity

analysis aimed to assess the influence of the Strouhal number St and the dimensionless forcing parameter F_x on the local positive and negative relative wave extrema $\Delta h_{ext}/h_0$, defined as the ratio of the maximum and the minimum value of the local free surface level variation to the initial still-water depth. The dimensionless duration $D^* = D(gh_0)^{1/2}/L$ of the excitation phase is assumed equal to approximately 3.13. Only the numerical results obtained at the left-hand side wall ($x = 0$) are discussed in the following. Fig. 7 shows the variation of the relative wave extrema with the Strouhal number for a fixed value of the forcing parameter ($F_x = 5$). Different values of St are obtained by changing the value of the forcing frequency ω. It can be noticed that positive extrema are systematically greater than the negative ones. For the smaller values of St, the negative wave extrema are equal to −1, which means that the minimum water depth at $x = 0$ is zero, and the seismic excitation is able to displace the water volume to the point of even temporarily drying up the bottom of the tank. Again from Fig. 7, it can be appreciated that relative wave extrema are highly sensitive to the seismic frequency and that the maximum positive wave amplitude grows significantly for St < 10, exceeding $2h_0$. Fig. 8 shows the influence of F_x for a fixed value of the Strouhal number (St ≅ 20) at $x = 0$. The value of the F_x parameter is changed by varying the value of the forcing acceleration amplitude A_x. As expected, the relative wave extrema increase monotonically with the intensity of the seismic disturbance. It is worth pointing out that wave extrema may occasionally occur in the first instants after the end of the excitation phase.

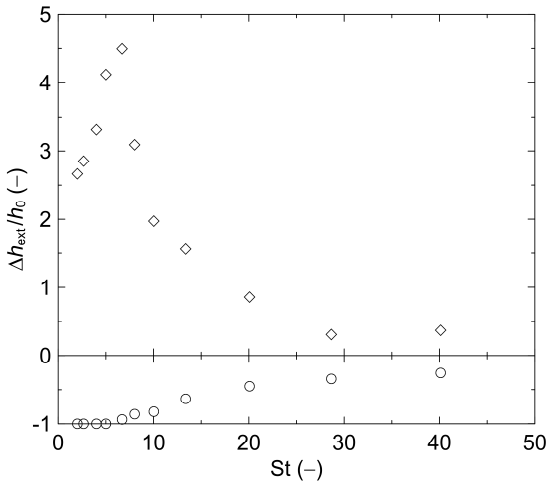

Fig. 7. Sinusoidally-forced water waves in a prismatic tank: influence of the Strouhal number on the positive (diamonds) and negative (circles) relative wave extrema at $x = 0$ ($F_x = 5$, $D^* = 3.13$).

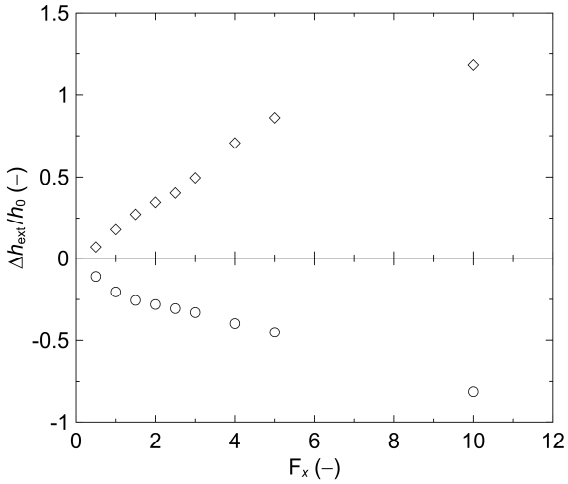

Fig. 8. Sinusoidally-forced water waves in a prismatic tank: influence of the dimensionless forcing parameter on the positive (diamonds) and negative (circles) relative wave extrema at $x = 0$ (St = 20.06, $D^* = 3.13$).

The capability of the numerical model to track moving wetting and drying fronts is assessed in the case of $A_x = 0.5g$ and $\omega = 2\pi/5$ rad/s ($F_x = 5$ and St ≅ 4). In this situation, the external sinusoidal acceleration is able to displace the water mass to the point of drying a portion of the bottom close to the left wall. The water depth threshold required by the wetting-drying numerical treatment by Aureli et al. [35] is assumed equal to 10^{-4} m in the numerical simulation. Figs. 9a and b show water depth and velocity numerical profiles at selected times. Moreover, Fig. 9c shows that the analytical path of the drying front originating at the left hand-side wall is satisfactorily tracked by the numerical model. However, it is worth noting that the predicted position of the drying front is very sensitive to the threshold value, as shown by Aureli et al. [35].

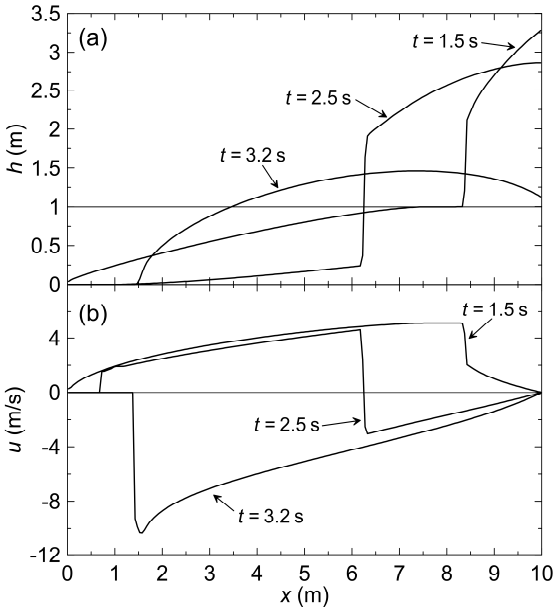

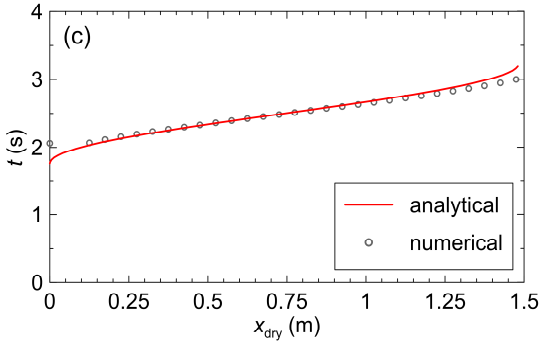

Fig. 9. Sinusoidally-forced oscillations in a prismatic tank ($L = 10$ m, $h_0 = 1$ m, $A_x = 0.5g$, $\omega = 2\pi/5$ rad/s): numerical profiles of water surface (a) and velocity (b) for selected times, and (c) comparison between analytical and numerical paths of the drying front ($\Delta x = \Delta y = 0.05$ m).

3.2. Seismic water waves in a rectangular open channel

The disturbance induced by a seismic-type action on an initially uniform open channel flow is analyzed in this section (see Fig. 10). To this aim, a 100 m long reach of a 10 m wide rectangular channel with horizontal bottom without resistance is considered, in which the flow (along the x direction) is initially uniform with water depth $h_0 = 2$ m and velocity $u_0 = 1$ m/s. Transmissive boundary conditions are assumed both at the upstream and downstream ends of the channel, so that the inlet and outlet do not disturb the propagation of the generated waves in the flow direction. The two cases of seismic acceleration parallel to the flow direction ($a_y = 0$) and perpendicular to the channel sides ($a_x = 0$) are investigated.

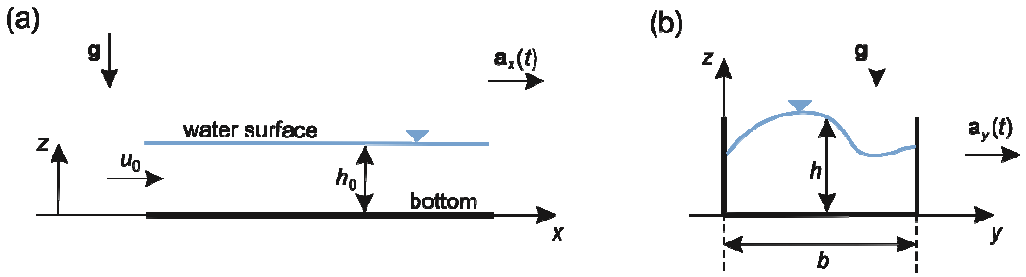

Fig. 10. Schematic of the problem of seismic-generated waves in a rectangular open channel: (a) longitudinal section; (b) cross-section.

The numerical simulations are performed on a Cartesian mesh with cell size $\Delta x = \Delta y = 0.1$ m, assuming $A_x = 0.5g$ (or $A_y = 0.5g$, depending on the case), $\omega = 2\pi$ rad/s, and $D = 10$ s. The Courant coefficient is set at 0.3, which allows obtaining $\mathrm{Nq} \cong 4 \cdot 10^2$ in the calculations. As for the case with external acceleration parallel to the flow direction, the water surface is not disturbed by the forcing excitation, whereas the flow velocity is uniformly affected by a periodic-in-time disturbance with the same frequency as the external acceleration. Fig. 11 compares numerical and analytical time series of both water height and flow velocity at a generic observation point in the channel. After the end of the external excitation, the previous undisturbed flow conditions are restored in the channel, because the duration of the sinusoidal forcing is assumed to be exactly equal to a multiple of the forcing period. However, the numerical model slightly underestimates the theoretical value of the streamwise velocity after the end of the excitation. The mean absolute error of the predicted flow velocity time series is $1.4 \cdot 10^{-2}$ m/s in the interval [0, 12] s, in which the numerical solution is discretized by $4.85 \cdot 10^3$ time

steps. The good agreement between numerical results and exact solution proves that, due to the second-order accuracy, the model does not introduce a significant amount of numerical diffusion, although a low value of the Courant number coefficient is used.

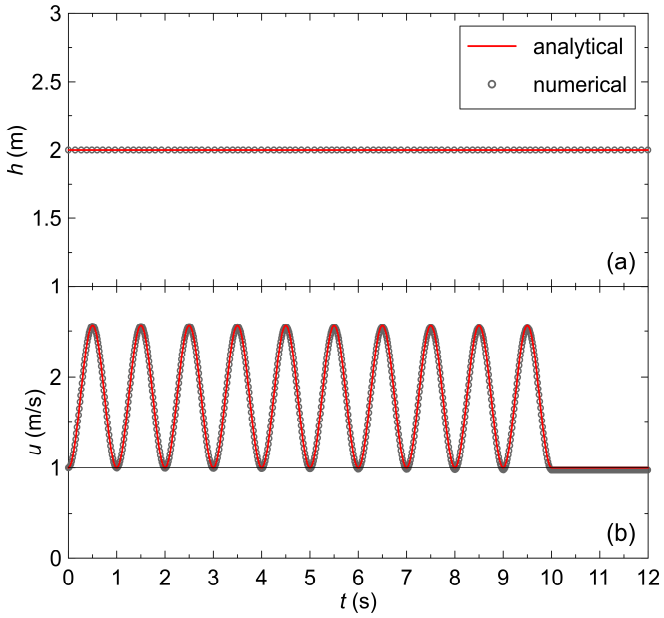

Fig. 11. Sinusoidally-forced water waves in a rectangular open channel: comparison between analytical and numerical time series of water height (a) and velocity (b) for a forcing excitation in the flow direction ($h_0 = 2$ m, $u_0 = 1$ m/s, $A_x = 0.5g$, $\omega = 2\pi$ rad/s, $D = 10$ s; $\Delta x = \Delta y = 0.1$ m). Only a subset of the numerical points is represented for clarity.

In the latter case, in which the external forcing acts orthogonally to the direction of flow, water sloshes back and forth across the channel, and a component of velocity in the transverse direction y arises. Maranzoni and Mignosa [43] observed that the flow variables do not change with x, and the u-velocity preserves the initial undisturbed value u_0 in the whole flow field. These peculiar flow features are captured by the numerical simulation. As an example, Figs. 12a and b show the water depth and transverse velocity numerical contour maps, respectively, at selected time $t = 1$ s for the following values of the forcing parameters: $A_y = 0.5g$, $\omega = 2\pi$ rad/s, and $D = 10$ s. The cross-sectional profiles of the flow variables are reported in panels c and d of Fig. 12.

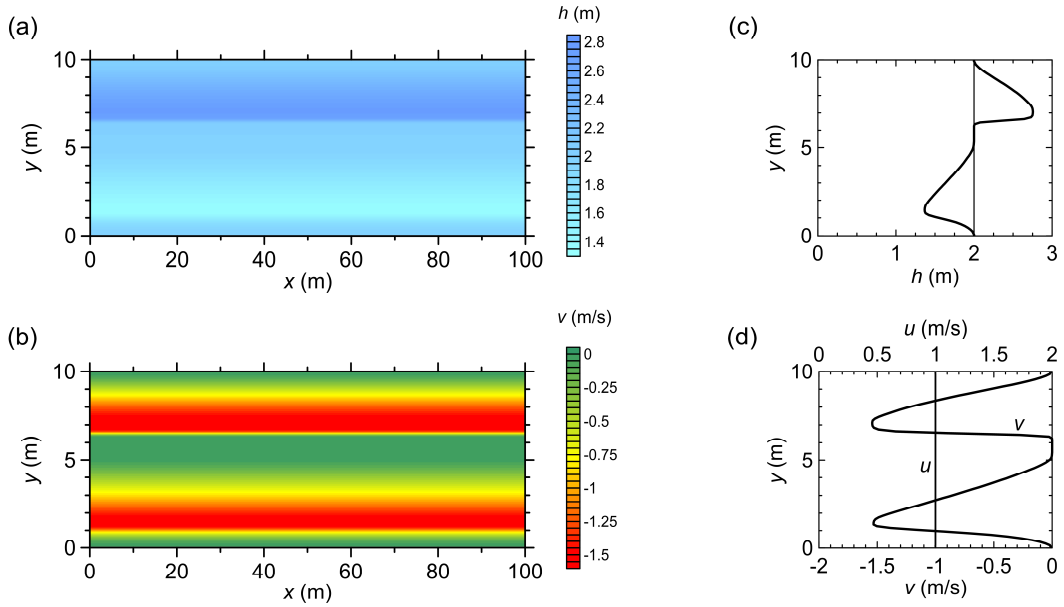

Fig. 12. Sinusoidally-forced water waves in a rectangular open channel: numerical contour maps of water depth (a) and y-velocity (b), cross-sectional profiles of water depth (c), cross-sectional profiles of x- and y-velocities (d) at selected time $t = 1$ s for a forcing excitation normal to the flow direction ($h_0 = 2$ m, $u_0 = 1$ m/s, $A_y = 0.5g$, $\omega = 2\pi$ rad/s, $D = 10$ s; $\Delta x = \Delta y = 0.1$ m).

3.3. Seismic water waves in a parabolic basin

The last numerical test concerns a seismic-generated sloshing in a frictionless parabolic basin with equation:

$$z_b(x,y) = h_0 \frac{x^2 + y^2}{L^2}, \tag{8}$$

in which z_b is the bottom elevation with reference to a horizontal plane and L is the radius at $z_b = h_0$ (Fig. 13). A water volume initially at rest, with free surface elevation h_0 above the vertex of the parabolic basin, is disturbed by a horizontal excitation along the x-direction varying in time according to Eq. (3). The features of the induced oscillations, involving wetting and drying moving fronts, are described in detail by Maranzoni and Mignosa [43], who obtained a dimensionless exact solution of the problem.

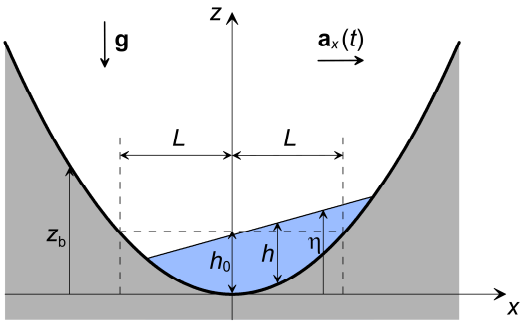

Fig. 13. Definition sketch for the problem of sinusoidally-forced sloshing in a parabolic basin.

The numerical simulation of this test case is performed using the following set of parameter values: $h_0 = 0.5$ m, $L = 2.5$ m, $A_x = 0.5g$, $\omega = 2\pi$ rad/s, $D = 10$ s. The solution domain is discretized with Cartesian cells of size $\Delta x = \Delta y = 0.02$ m. The wetting-drying water depth threshold is assumed equal to 10^{-5} m, and the Courant coefficient is set at 0.9. This last choice guarantees that the Nyquist number of the computations is greater than $2 \cdot 10^2$, largely satisfying the antialiasing condition.

The numerical results reported in Fig. 14a for a selected time show that the computed water surface is almost planar and the velocity field is nearly uniform, which matches the analytical solution. Moreover, Fig. 14b shows that numerical and analytical water surface profiles along the x-axis at selected times agree very well. MAE is equal to $6.2 \cdot 10^{-4}$ m for the water surface profiles at $t = 0.5$ s and $t = 1$ s, while it is equal to $1.3 \cdot 10^{-3}$ m for the profile at $t = 3$ s. Fig. 15 compares the numerical and analytical water depth and velocity times series at observation points (0, 0) and (2.2, 0) (Figs 14a and 14b, respectively). The former point is never crossed by the shoreline, whereas the latter gets dry and wet during the sloshing motion. The numerical model provides an overall good reproduction of the analytical time series, despite the tendency of slightly overestimating the flow velocities (which are derived quantities) close to the drying front. The model MAE in predicting the time evolution of water depth in the excitation phase ($0 \le t \le D = 10$ s) is equal to $9.1 \cdot 10^{-4}$ m at point (0, 0) and $2.7 \cdot 10^{-3}$ m at point (2.2, 0); MAEs of the numerical velocity time histories are $1.3 \cdot 10^{-2}$ m/s and $1.9 \cdot 10^{-2}$ m/s, respectively. The predicted shoreline is almost circular (Fig. 14a) and its motion along the x axis accurately follows the analytical one for $0 \le t \le D$ (see Fig. 16) with a mean absolute error of $2.4 \cdot 10^{-2}$ m, which is in the grid size order of magnitude.

The maximum run-up achieved during the oscillating motion depends on both the amplitude and frequency of the earthquake. Based on the dimensionless exact solution of the problem, Maranzoni and Mignosa [43] derived the expression of the dimensionless maximum run-up $R^*_{1\max}$ along the x-axis during the first oscillation

as a function of the dimensionless parameters F_x and St. Fig. 17 shows the comparison between analytical and numerical dimensionless run-up heights for some values of St, with $F_x = 2.5$ ($A_x = 0.5g$). Different values of St ranging from 0.47 to 9.46 are obtained by changing the forcing period value in the range [0.75 s, 15 s]. The special values of $(2)^{1/2}$ and 0.873 are also considered for St, which correspond to the two notable situations in which the forcing frequency equals the natural frequency and the maximum run-up is expected, respectively [43]. However, it is worth noting that too low values of St (namely smaller than 3 in this test case) correspond to forcing periods which are not plausible for a realistic seismic excitation. In Fig. 17 the numerical results fit the analytical solution well, confirming the capability of the model to track wetting and drying fronts.

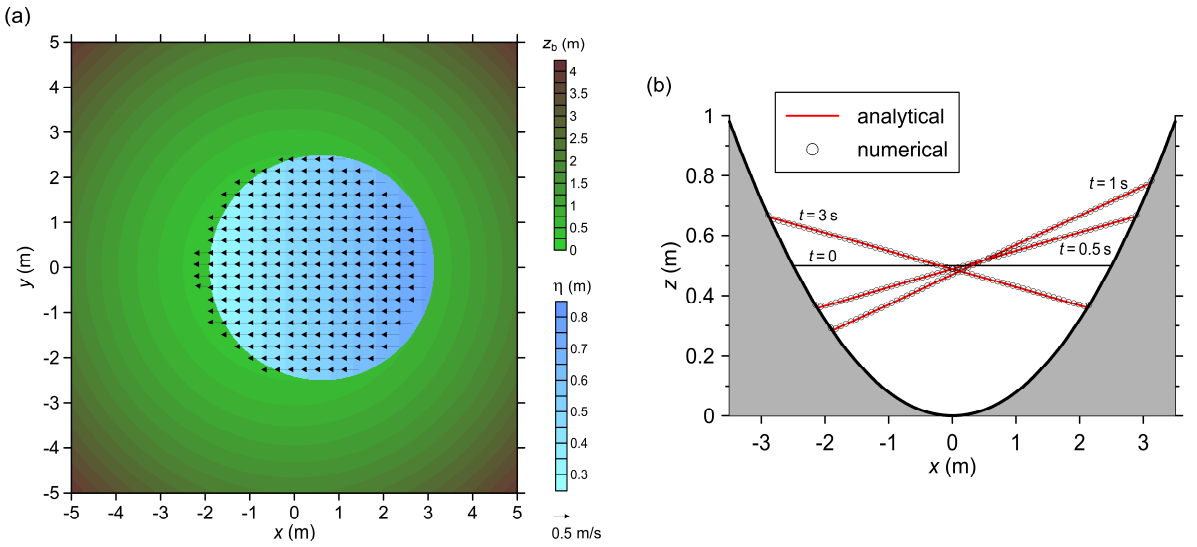

Fig. 14. Sinusoidally-forced oscillations in a parabolic basin: (a) numerical flow field at $t = 1$ s; (b) slice of analytical and numerical water surfaces along the x-axis for selected times ($h_0 = 0.5$ m, $L = 2.5$ m, $A_x = 0.5g$, $\omega = 2\pi$ rad/s, $D = 10$ s; $\Delta x = \Delta y = 0.02$ m). Only a subset of the numerical points and vectors are represented for clarity.

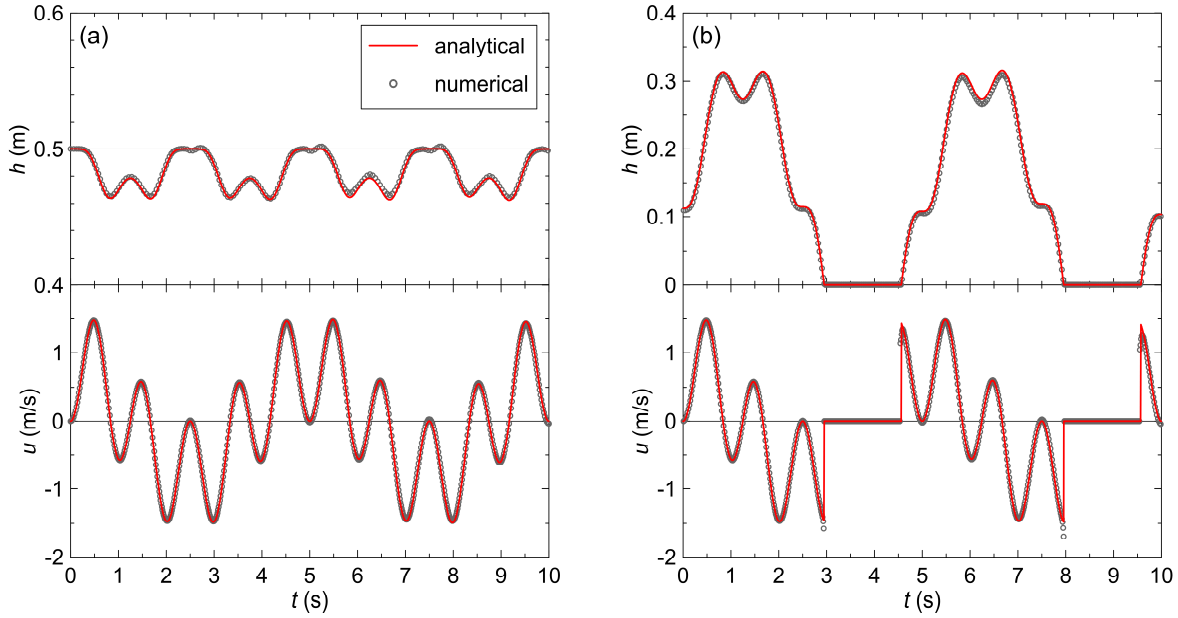

Fig. 15. Sinusoidally-forced oscillations in a parabolic basin: comparison between analytical and numerical time series of water depth and u-velocity component for two selected observation points: (a) $x = 0$, $y = 0$; (b) $x = 2.2$ m, $y = 0$ ($h_0 = 0.5$ m, $L = 2.5$ m, $A_x = 0.5g$, $\omega = 2\pi$ rad/s, $D = 10$ s; $\Delta x = \Delta y = 0.02$ m). Only a subset of the numerical points is represented for clarity.

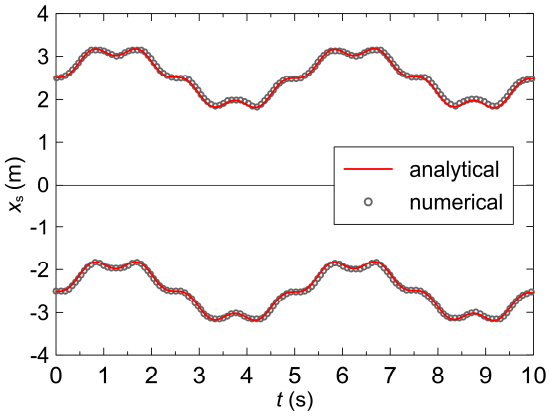

Fig. 16. Sinusoidally-forced oscillations in a parabolic basin: comparison between analytical and numerical time histories of the shoreline position along the x-axis ($h_0 = 0.5$ m, $L = 2.5$ m, $A_x = 0.5g$, $\omega = 2\pi$ rad/s, $D = 10$ s; $\Delta x = \Delta y = 0.02$ m). Only a subset of the numerical points is represented for clarity.

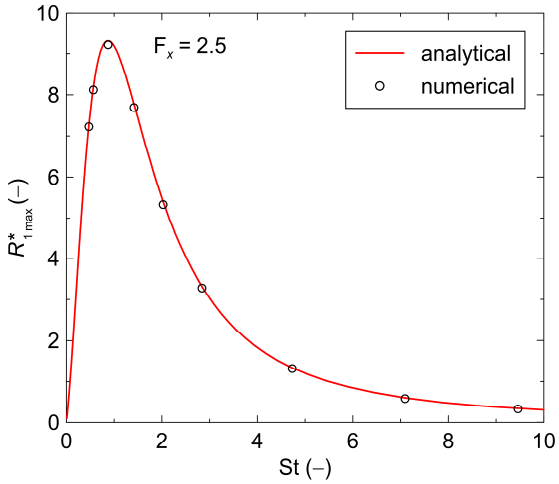

Fig. 17. Sinusoidally-forced oscillations in a parabolic basin: comparison between analytical and numerical dependences of the dimensionless maximum run-up during the first oscillation on the Strouhal number for $F_x = 2.5$ ($h_0 = 0.5$ m, $L = 2.5$ m, $A_x = 0.5g$; $\Delta x = \Delta y = 0.02$ m).

4. Validation of the model

In this section the numerical model is validated against some experimental data acquired by Antuono et al. [21] during a laboratory investigation on shallow water sloshing in a swaying or rolling rectangular tank. The tank was 1 m long and 0.1 m wide (refer to the sketch in Fig. 2), and was mounted on a suitable mechanical device able to transmit both sinusoidal sway and roll motions to the tank (see also [49]). The water depth was measured by capacitance transducers at four gauge points located at 0.05, 0.1, 0.2, and 0.3 m from the left-hand side wall. Of the various test conditions considered by Antuono et al. [21] to explore different breaking types, only the S1 sway motion condition is analyzed here, which concerns very shallow water depths and gives rise to moderate oscillations with bores. This test is characterized by 0.034 m initial water depth, 2.272 s^{-1} forcing frequency (corresponding to a period of approximately 2.765 s), and 0.176 m/s^2 acceleration amplitude in the longitudinal x-direction.

The numerical simulation is performed by discretizing the computational domain through square cells sized 0.002 m and neglecting friction. The Courant number coefficient is set at 0.9 and correspondingly the Nyquist number of the computations is in the order of 10^3.

Fig. 18 compares experimental and numerical time histories of water level variation at the four gauge points. Time is expressed in dimensionless form (t/T) in terms of number of forcing periods. The comparison is restricted to the steady state wave condition, which occurs after the end of the transient phase [21]. This flow condition was observed to occur after more than 40 excitation periods in the test considered here. The predicted time evolution of water surface displacement at the selected gauge points shows overall good agreement with the

experimental data. In particular, the timing and shape of the water level hydrographs are well reproduced by the numerical model, as well as the typical sawtooth waveform of moving bores, which is fairly pronounced at the gauge points located at $x = 0.20$ m and $x = 0.30$ m. The predicted positive wave peaks compare well with the measured ones, even if a slight underestimation can be noticed at $x = 0.10$ m and $x = 0.30$ m. The height of the secondary peaks preceding the maximum ones is also slightly underestimated. On the other hand, the amplitude of the negative oscillations is systematically overestimated by the numerical model; such behaviour is also shown by the numerical results presented in Antuono et al. [21]. The numerical results are free of spurious oscillations.

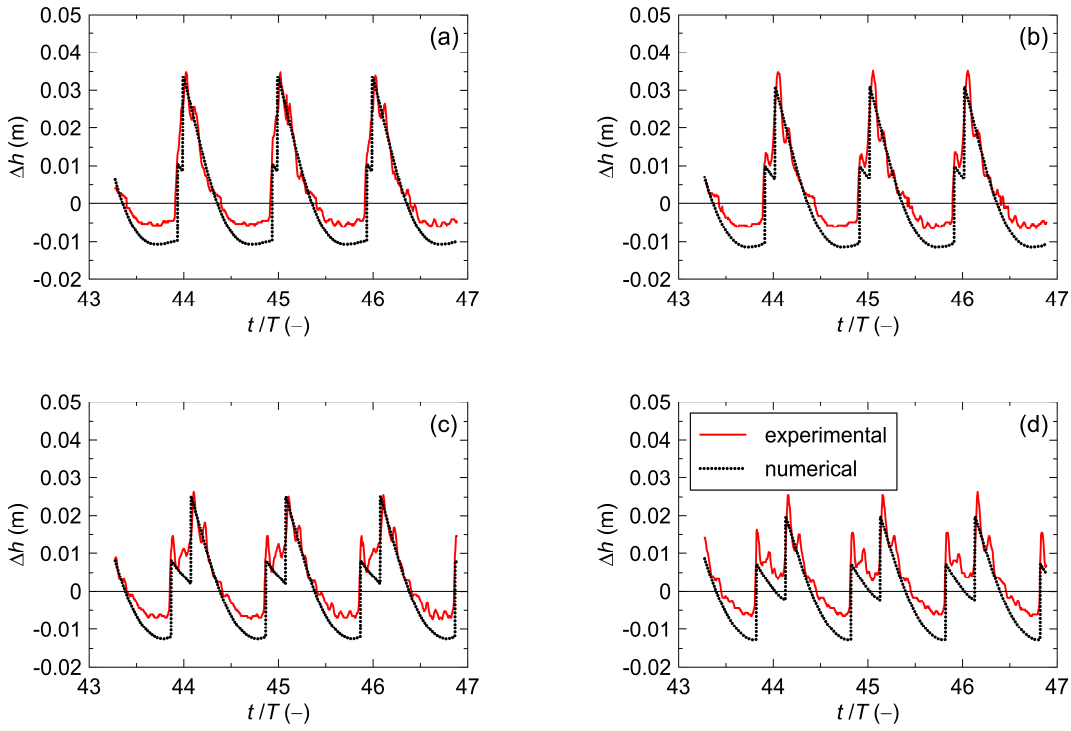

Fig. 18. S1 sway motion test by Antuono et al. [21]: comparison between experimental and numerical water level variation time series at $x = 0.05$ m (a), $x = 0.10$ m (b), $x = 0.20$ m (c), $x = 0.30$ m (d).

5. Applications

5.1 Reservoir formed by a dam

In this subsection the numerical model is applied to a real-field case concerning the propagation of water waves induced by a seismic-type excitation in the lake created by the Mignano dam, a concrete gravity dam located in Northern Italy, in the upper course of the Arda River (a right-bank tributary of the Po River). The maximum water depth of the Mignano reservoir is 45 m, with a total storage capacity of $15.5 \cdot 10^6$ m^3 and a surface area of approximately 0.85 km^2 [50–52]. At the maximum storage level (340.5 m a.s.l.), the average

water depth is approximately equal to 16.3 m and the lake is approximately 2.8 km long from the dam face to the opposite side. Fig. 19 shows the contour map of the lake bathymetry.

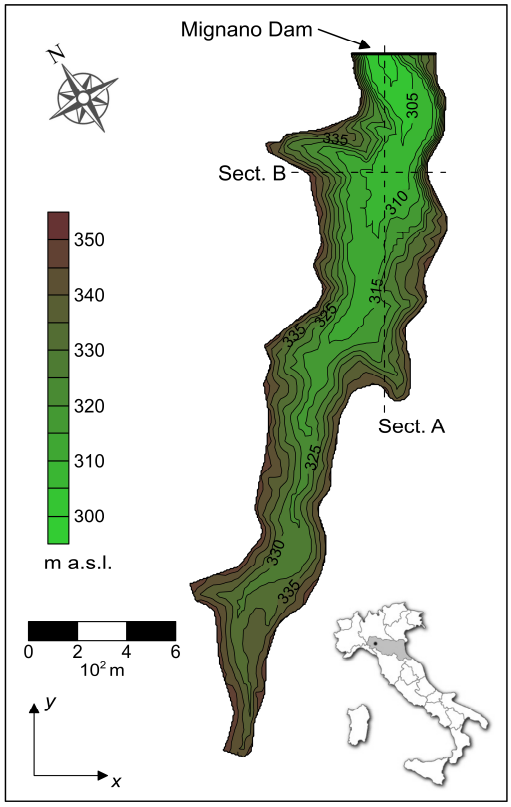

Fig. 19. Bathymetry of the lake created by the Mignano dam.

It is assumed that the water stored in the reservoir (supposed initially at rest at the maximum storage level) is disturbed by 20 s horizontal acceleration varying sinusoidally in time with $0.2g$ amplitude, which is the seismic peak ground acceleration (with a return period of approximately 1425 years, corresponding to the life safety performance level) for the area of interest, according to the Italian seismic hazard map. The reservoir being initially full is a precautionary hypothesis, since the occurrence of a strong earthquake when the reservoir is filled to its maximum water level is quite improbable [2]. Two scenarios are considered, i.e. the forcing acceleration is assumed to be either normal (Scenario 1) or parallel (Scenario 2) to the dam, with periods ranging from 0.5 to 2 s. The numerical simulations are performed on a Cartesian mesh with cell size $\Delta x = \Delta y = 5$ m, and are extended for a total time of 2 min in order to predict the effects of the seismic disturbance during the first stages after the end of the external excitation. Since historical data for the calibration of the Manning roughness coefficient are lacking, n is assumed equal to 0.06 $m^{-1/3}s$; this value is suitable for mountain valleys with irregular side slopes and bottom (e.g. [53]). In any case, the effect of friction is expected to be quite irrelevant in

a sloshing process, which is mainly affected by inertia, except near wetting-drying boundaries. The wetting-drying water depth threshold is set at 10^{-3} m, while the Courant number coefficient is set at 0.2, which ensures that aliasing problems are prevented in the time discretization of the forcing source term, at least for the periods investigated. The dam is represented as a rigid solid wall with unlimited height and identifies the only (reflective-type) boundary condition imposed in the computational domain.

The main results of the computations are reported in Table 1 in terms of maximum water level increase behind the dam (at the location where the thalweg of the river intersects the dam), additional flooded areas (with reference to the undisturbed lake surface area), and maximum run-up height at the lake sides. The cases in which the maximum water level increase at the dam exceeds the freeboard available are highlighted in bold in Table 1. For all the simulations, Nq is greater than 20, thus the assumed antialiasing condition is always satisfied with the adopted value of Cr. The results show that seismic-type excitations with longer periods are more dangerous and that a sinusoidal disturbance with $0.2g$ amplitude and 1.5-2 s period is potentially capable of causing dam overtopping.

As an example of numerical results, Fig. 20 shows a perspective view of the predicted water surfaces at $t = 10$ s for the two scenarios considered, and a forcing period of 1 s ($\omega = 2\pi$ rad/s), together with the corresponding water surface profiles at the two sections indicated in Fig. 19. In the first scenario, a positive wave originates at the dam and spreads backwards in the reservoir (Figs. 20a and b), whereas in the second scenario the run-up on the lake edge induces a wave which propagates towards the opposite side of the lake (Figs. 20c and d). Fig. 21 shows the numerical time series of water level variation at the intersection between the river thalweg and the dam for the two different scenarios, again with a forcing period of 1 s. In the case of a seismic action normal to the dam (Scenario 1), the predicted water levels oscillate in time with the forcing frequency during the excitation phase ($t \leq 20$ s). The maximum rise in the water level is attained in this phase. After the end of the forcing action, the oscillating motion is characterized by a lower water level excursion and a longer period. On the other hand, for an excitation parallel to the dam (Scenario 2), the maximum water level increase is comparable to that predicted in Scenario 1 and occurs after the end of the excitation phase, at the transit of the positive wave originated at the lake side.

Table 1. Water waves induced by a sinusoidal excitation in Lake Mignano: sensitivity analysis on the forcing period.

Scenario	Excitation period (s)	Nyquist number (–)	Water level increase at the dam (m)	Flooded area increase (%)	Run-up height on the lake sides (m)

Excitation normal to the dam ($A_y = 0.2g$)	0.5	~ 20	0.41	1.02	1.28
	0.75	~ 30	0.75	1.13	1.89
	1.0	~ 40	1.13	2.06	2.34
	1.5	~ 60	**1.90**	2.22	3.18
	2.0	~ 80	**2.63**	3.96	4.36
Excitation parallel to the dam ($A_x = 0.2g$)	0.5	~ 20	0.54	1.76	2.52
	0.75	~ 30	0.30	1.55	1.81
	1.0	~ 40	1.09	3.81	4.74
	1.5	~ 60	0.72	3.13	3.26
	2.0	~ 80	**2.19**	7.44	8.19

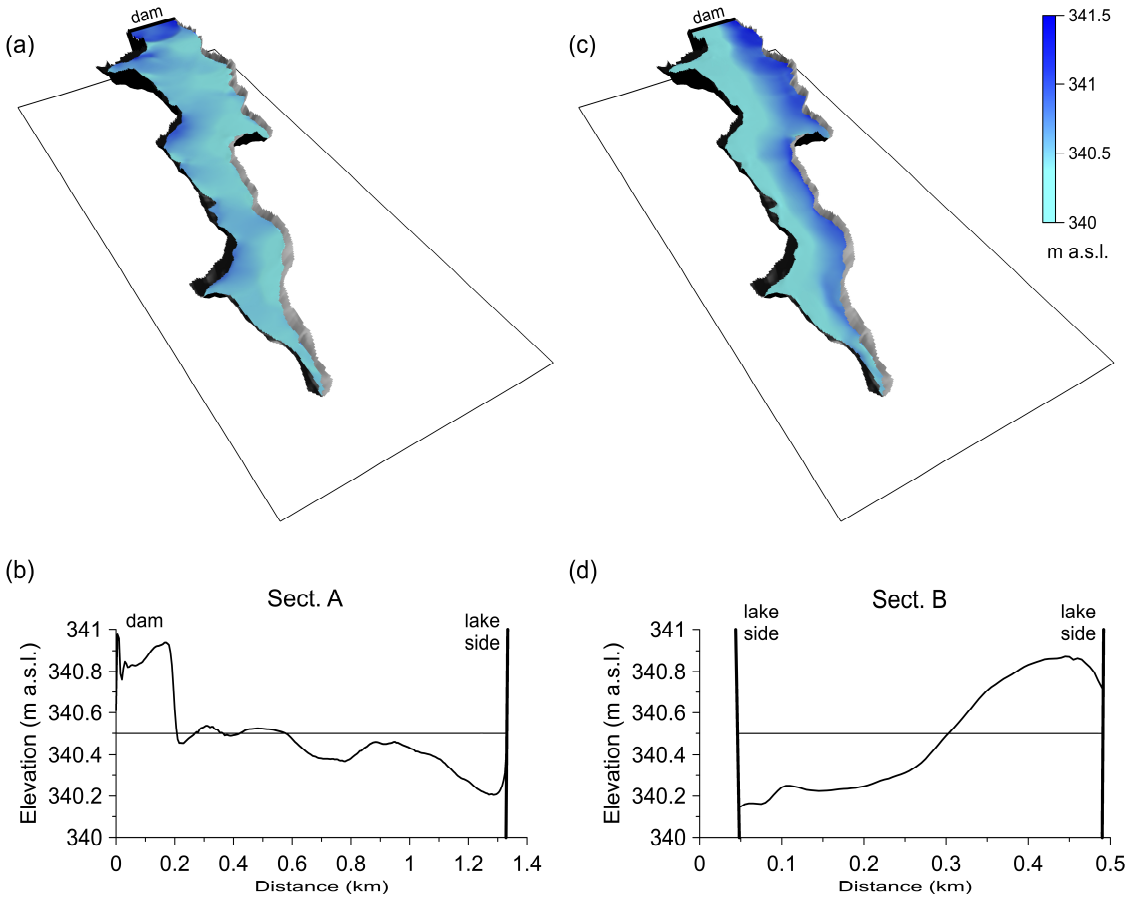

Fig. 20. Perspective view of the water surface waves induced by a sinusoidal excitation in Lake Mignano, and water surface profiles at Sections A and B indicated in Fig. 19 at selected time $t = 10$ s: forcing acceleration normal to the dam (a, b); forcing acceleration parallel to the dam (c, d). (Amplitude of the forcing acceleration: $0.2g$; excitation period: 1 s; duration of the excitation: 20 s.)

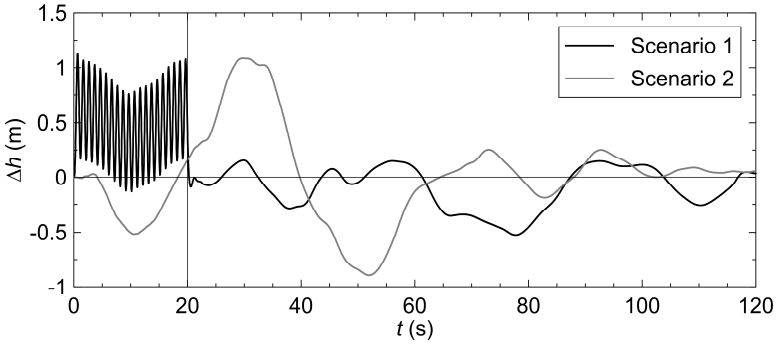

Fig. 21. Numerical time series of water level variation at the dam site for the two excitation scenarios considered (amplitude of the forcing acceleration: 0.2*g*; excitation period: 1 s; duration of the excitation: 20 s).

The response of Lake Mignano to real seismic excitation is analyzed in the following. To this aim, seismic acceleration records including the acceleration components in two orthogonal horizontal directions are considered, namely the N-S and E-W accelerograms measured at Forca Canapine Station during the recent 2016 earthquake in Central Italy [54]. It is hypothesized that the N-S and E-W accelerograms act simultaneously along the directions normal and parallel to the dam, respectively. A 20 s time interval is selected, in which the recorded seismic acceleration is significant (see Figs. 18a and b). The numerical simulation is performed on the same grid described above and is extended for a total time of 1 min. The Courant number coefficient is set at 0.1 in order to accurately reproduce the acceleration time series available, provided with time resolution of 0.005 s. The predicted water surface fluctuations at the location where the thalweg of the river intersects the dam are shown in Fig. 18c. A maximum water level increase of 0.71 m is expected at the dam site as a result of this specific seismic excitation.

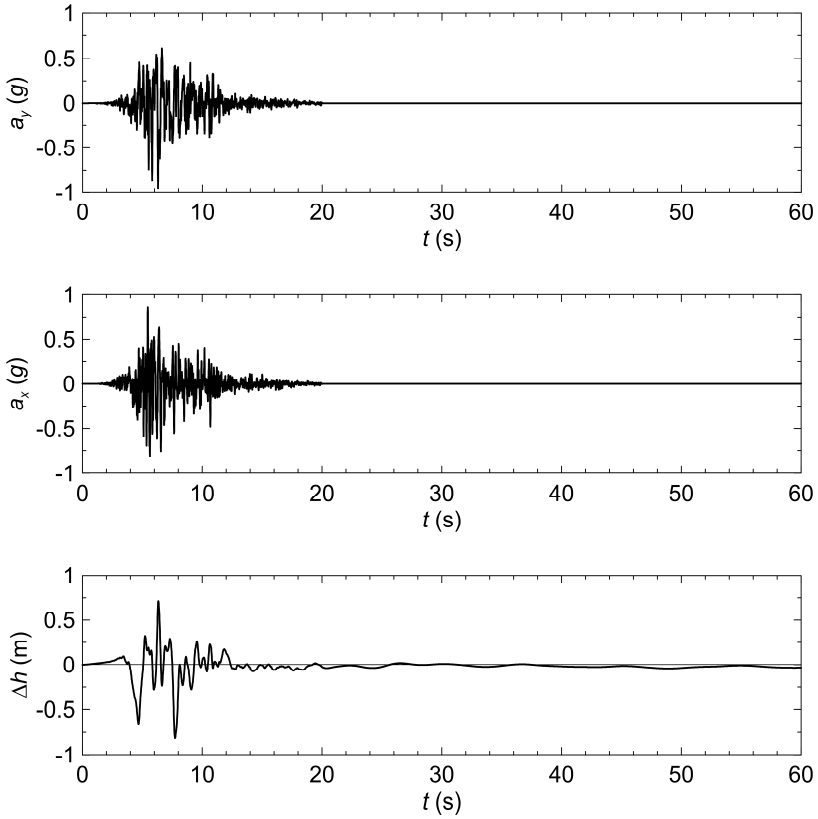

Fig. 22. Numerical modelling of the water waves induced by real seismic excitation in the Mignano reservoir: (a) component accelerogram in the direction normal to the dam; (b) component accelerogram in the direction parallel to the dam; (c) predicted water surface fluctuations at the dam site.

5.2 Storage tank of a water supply system

The application of the numerical model to the simulation of seismic-generated waves in a real tank for storing drinking water is presented in this subsection. An underground storage reservoir of the water supply system of the town of Parma (Northern Italy), denominated "Giovanardi" tank, is considered. This facility is a prismatic concrete structure with a flat bottom, having a quadrilateral base with an area of approximately 845 m^2 and a height of 4.6 m. A system of square pillars sized 0.4 m supports 0.45 m high beams on which the plane ceiling rests. Fig. 23 reports the plan view sketch of the facility.

The water (initially at rest) contained in the storage tank is disturbed by sinusoidal acceleration with a 0.3g design amplitude (which is the seismic peak ground acceleration corresponding to a return period of 1900 years, according to the Italian technical regulations) and a period of 1 s, acting along either the x or y direction (see Fig. 23), for a duration of 20 s. Initial water depths of 2 and 4 m are considered, which correspond to the minimum and maximum depths in the normal operating conditions, respectively.

A Cartesian mesh with square cells sized 0.05 m is adopted in the simulations. The Manning roughness coefficient is set at 0.013 $m^{-1/3}s$, owing to the very smooth surface of the reservoir's concrete walls [53]. The Courant number coefficient is set at 0.9, which ensures that the numerical solution advances with a Nyquist number abundantly greater than 10^2 in the simulations performed.

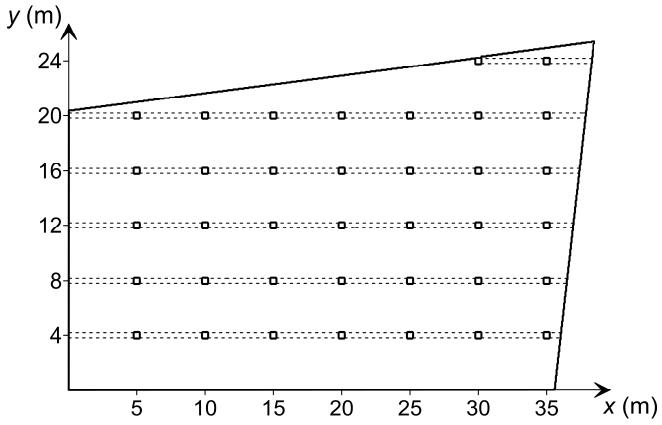

Fig. 23. Plan view of the "Giovanardi" storage tank (water supply system of the town of Parma, Italy). The traces of the beams supporting the ceiling of the tank are reported in dashed lines.

As an example of numerical results, Fig. 24 shows the predicted water depth and velocity fields at $t = 5$ s for the two forcing directions considered, when the initial water depth h_0 is equal to 2 m. In both situations, the flow fields are very complex and show marked 2D features, due to the multiple reflections against the pillars and the lateral walls, especially those arranged obliquely with reference to the hypothesized directions of the seismic excitation. Moreover, for $h_0 = 2$ m, the predicted maximum water level increase is in the order of 1 m, and thus the water surface never reaches the ceiling of the covered tank. However, the possibility that a portion of the ceiling goes under pressure, with a consequent simultaneous presence of free surface and pressurized flow regimes, cannot be excluded a priori. In the case study considered here, this occurs, for example, when the initial water level in the tank is maximum ($h_0 = 4$ m) and the seismic disturbance has the characteristics described above. In such a case, the 2D generalization of the Preissmann slot concept proposed by Maranzoni et al. [46] and Maranzoni and Mignosa [55] can be exploited to correctly model this peculiar flow condition. As an example, Fig. 25 shows computed piezometric head profiles (with reference to the bottom of the tank) along selected sections at $t = 3$ s, for the case of $h_0 = 4$ m and a seismic excitation in either the x- or y-direction. It can be noted that pressurized flow occurs only at the beams and in small regions close to the pillars. In the calculations concerning this case, the widths of the Preissmann slots along the x and y directions are assumed equal to $\Delta y/100$ and $\Delta x/100$, respectively.

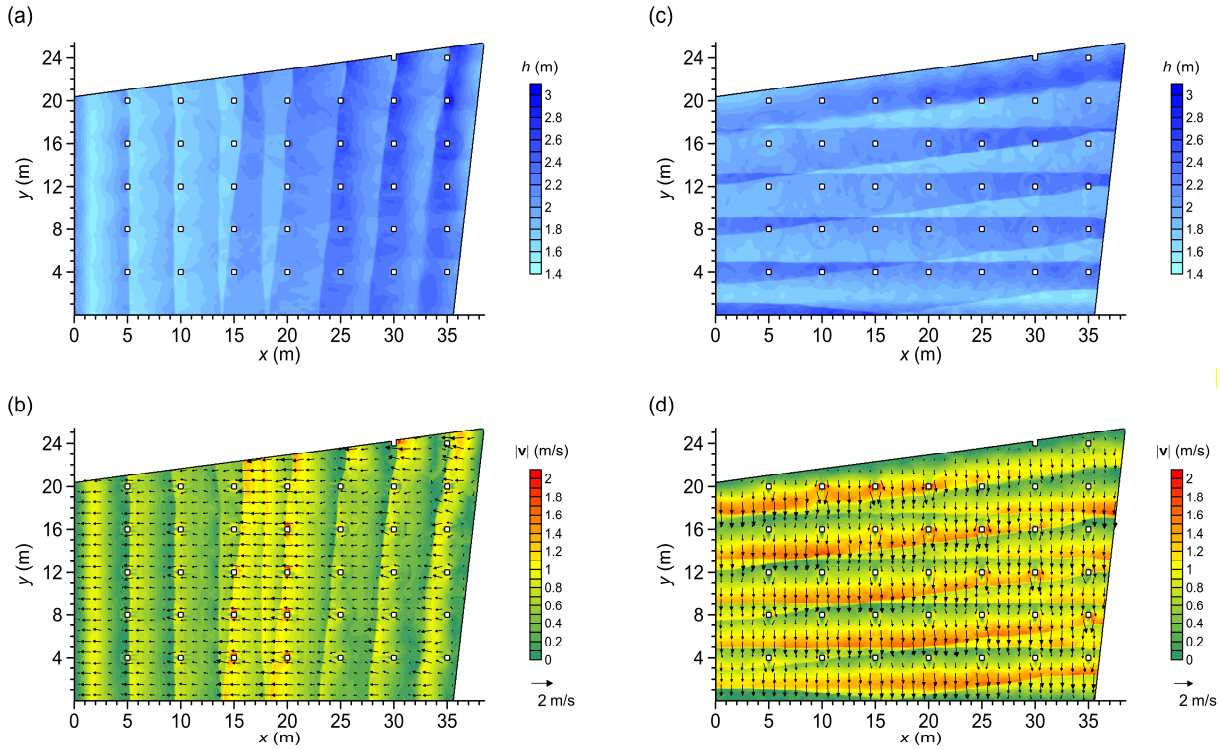

Fig. 24. Example of numerical results obtained for the case study of sinusoidally-forced water waves in the "Giovanardi" storage tank: water depth contour maps and velocity fields at $t = 5$ s for forcing acceleration in the x (a, b) and y (c, d) directions in the case of $h_0 = 2$ m (amplitude of the forcing acceleration: $0.3g$; excitation period: 1 s). Only a subset of the numerical velocity vectors is represented for clarity.

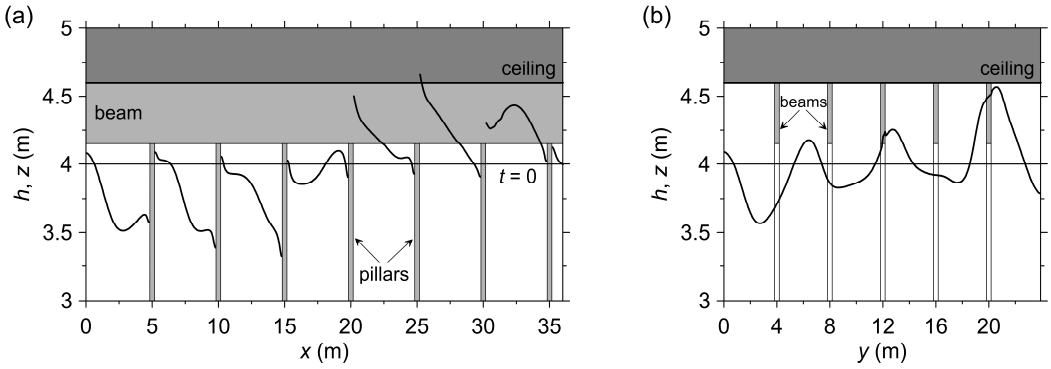

Fig. 25. Numerical piezometric head profiles along selected sections at $t = 3$ s for sinusoidal excitation with $0.3g$ amplitude and 1 s period, in the case of $h_0 = 4$ m: (a) section $y = 4$ m and forcing acceleration in the x-direction; (b) section $x = 27.5$ m and forcing acceleration in the y-direction.

6. Conclusions

In this paper finite-amplitude water waves generated by a horizontal seismic-type disturbance are modelled by the 2D depth-averaged shallow water equations, in which a sinusoidal time-varying source term is added in

order to represent the forcing effect due to an essentially undulatory earthquake.

The numerical tests show that a finite volume high-resolution scheme, coupled with a splitting pointwise treatment of the source term, is an effective and robust computational tool to integrate the governing equations. Actually, the numerical model used in this work can accurately reproduce exact solutions of theoretical sloshing problems involving smooth waves, even with wetting and drying, as confirmed by the estimates of the numerical errors based on the mean absolute error. Adopting a suitable antialiasing condition in the computations based on the Nyquist number can guarantee accurate time discretization of the oscillating forcing term. The sensitivity analysis on the influential dimensionless parameters performed in the test case of oscillations in a prismatic tank shows that the relative wave extrema are very sensitive on the Strouhal number (especially the positive wave extrema) and increase with the dimensionless forcing parameter representing the amplitude of the exciting acceleration.

The comparison of model results with experimental data available in literature on shallow water sloshing in a swaying rectangular tank confirms the effectiveness of the numerical model in predicting sloshing phenomena in shallow water conditions, even in the presence of bores.

Finally, the simulations of water waves induced by both sinusoidal and real seismic horizontal acceleration in real storage reservoirs prove that the model can be effectively used in field-scale applications and can provide useful information about the freeboards which need to be ensured in order to provide a suitable margin of safety during an earthquake.

Acknowledgements

The authors kindly acknowledge Dr. J. Hinks for the useful discussion, Dr. M. Antuono for providing the experimental data used for the validation of the numerical model, and IRETI S.p.A. for providing the dimensional data of the “Giovanardi” water tank. The Editors and Reviewers are kindly acknowledged too for their valuable, constructive comments, which have greatly contributed to the improvement of the paper.

References

[1] FEMA, Federal Guidelines for Dam Safety: Earthquake Analyses and Design of Dams, United States Department of Homeland Security, USA, 2005.

[2] J.L. Hinks, Y. Kitamura, A.T. Murphy, Risk analyses for large dams, in: R.M. Gunn, M. Balissat, P.

Manso, L. Mouvet, A. Schleiss (Eds.), Proceedings of 13th ICOLD Benchmark Workshop on the Numerical Analysis of Dams, Switzerland, 2015, pp. 277–284.

[3] A.J. Yarde, L.S. Banyard, N.W.H. Allsop, Reservoir Dams: Wave Conditions, Wave Overtopping and Slab Protection, Report SR 459, HR Wallingford, Wallingford, UK, 1996.

[4] MIT, Italian Ministry of Infrastructures and Transport, Decree June 26, 2014, Norme tecniche per la progettazione e la costruzione degli sbarramenti di ritenuta (dighe e traverse) [Technical regulations on dam planning and building], 2014 (in Italian).

[5] ICE, Floods and Reservoir Safety, fourth ed., Institution of Civil Engineers Publishing, UK, 2015.

[6] A. McGarr, Excitation of seiches in channels by seismic waves, J. Geophys. Res. 70 (4) (1965) 847–854. https://doi.org/10.1029/JZ070i004p00847.

[7] A. McGarr, R.C. Vorhis, Seismic Seiches from the March 1964 Alaska Earthquake, Geological Survey Professional Paper 544-E, United States Department of the Interior, Washington, USA, 1968.

[8] A.B. Rabinovich, Seiches and harbor oscillations, in: Y.C. Kim (Ed.), Handbook of Coastal and Ocean Engineering, World Scientific, Singapore, 2009, pp. 193–236. https://doi.org/10.1142/9789812819307_0009.

[9] W.L. Donn, Alaskan earthquake of 27 March 1964: remote seiche stimulation, Science 145 (3629) (1964) 261–262. https://doi.org/10.1126/science.145.3629.261.

[10] A. Barberopoulou, A. Qamar, T.L. Pratt, W.P. Steele, Long-period effects of the Denali Earthquake on water bodies in the Puget lowland: observations and modeling, Bull. Seism. Soc. Amer. 96 (2) (2006) 519–535. https://doi.org/10.1785/0120050090.

[11] C. Scawthorn, Lifeline performance, in: C. Scawthorn (Ed.), The Marmara, Turkey Earthquake of August 17, 1999: Reconnaissance Report, MCEER-00-0001, Multidisciplinary Center for Earthquake Engineering Research, Buffalo, New York, USA, 2000, pp. 109–117.

[12] J.L. Hinks, E.M. Gosschalk, Dams and earthquakes – a review, Dam Engineering 4 (1) (1993) 9–26.

[13] G.W. Housner, Dynamic pressures on accelerated fluid containers, Bull. Seismol. Soc. Am. 47 (1) (1957) 15–35.

[14] B. Hunt, N. Priestley, Seismic water waves in a storage tank, Bull. Seismol. Soc. Am. 68 (2) (1978) 487–499.

[15] B. Hunt, Seismic-generated water waves in axisymmetric tanks, J. Eng. Mech. 113 (5) (1987) 653–670. https://doi.org/10.1061/(ASCE)0733-9399(1987)113:5(653).

[16] Y.S. Choun, C.B. Yun, Sloshing characteristics in rectangular tanks with a submerged block, Comput. Struct. 61 (3) (1996) 401–413. https://doi.org/10.1016/0045-7949(96)00084-3.

[17] T.G. Lepelletier, F. Raichlen, Nonlinear oscillations in rectangular tanks, J. Eng. Mech. 114 (1) (1988) 1–23. https://doi.org/10.1061/(ASCE)0733-9399(1988)114:1(1).

[18] T. Okamoto, M. Kawahara, Two-dimensional sloshing analysis by Lagrangian finite element method, Int. J. Numer. Meth. Fluids 11 (5) (1990) 453–477. https://doi.org/10.1002/fld.1650110502.

[19] P. Heinrich, Nonlinear water waves generated by submarine and aerial landslides, J. Waterw. Port Coast. Ocean Eng. 118 (3) (1992) 249–266. https://doi.org/10.1061/(ASCE)0733-950X(1992)118:3(249).

[20] K.C. Biswal, S.K. Bhattacharyya, P.K. Sinha, Non-linear sloshing in partially filled containers with baffles, Int. J. Numer. Meth. Eng. 68 (3) (2006) 317–337. https://doi.org/10.1002/nme.1709.

[21] M. Antuono, A. Bardazzi, C. Lugni, M. Brocchini, A shallow-water sloshing model for wave-breaking in rectangular tanks, J. Fluid Mech. 746 (2014) 437–465. https://doi.org/10.1017/jfm.2014.127.

[22] P.K. Mohapatra, M.H. Chaudhry, Numerical solution of Boussinesq equations to simulate dam-break flows, J. Hydraul. Eng., 130 (2) (2004) 156–159. https://doi.org/10.1061/(ASCE)0733-9429(2004)130:2(156).

[23] B.J. Dewals, S. Erpicum, P. Archambeau, S. Detrembleur, M. Pirotton, Depth-integrated flow modelling taking into account bottom curvature, J. Hydraul. Res. 44 (6) (2006) 785–795. https://doi.org/10.1080/00221686.2006.9521729.

[24] R. Cienfuegos, E. Barthélemy, P. Bonneton, A fourth-order compact finite volume scheme for fully nonlinear and weakly dispersive Boussinesq-type equations. Part I: Model development and analysis, Int. J. Numer. Meth. Fluids, 51 (11) (2006) 1217–1253. https://doi.org/10.1002/fld.1141.

[25] M. Zijlema, G. Stelling, P. Smit, SWASH: An operational public domain code for simulating wave fields and rapidly varied flows in coastal waters, Coast. Eng. 58 (10) (2011) 992–1012. https://doi.org/10.1016/j.coastaleng.2011.05.015.

[26] A. Viviano, R.E. Musumeci, E. Foti, A nonlinear rotational, quasi-2DH, numerical model for spilling wave propagation, Appl. Math. Model. 39(3–4) (2015) 1099–1118. https://doi.org/10.1016/j.apm.2014.07.030.

[27] F.N. Cantero-Chinchilla, O. Castro-Orgaz, S. Dey, J.L. Ayuso, Nonhydrostatic dam break flows. I: Physical equations and numerical schemes, J. Hydraul. Eng. 142 (12) (2016) 04016068. https://doi.org/10.1061/(ASCE)HY.1943-7900.0001205.

[28] B. Tatlock, R. Briganti, R.E. Musumeci, M. Brocchini, An assessment of the roller approach for wave breaking in a hybrid finite-volume finite-difference Boussinesq-type model for the surf-zone, Appl. Ocean Res. 73 (2018) 160–178. https://doi.org/10.1016/j.apor.2018.01.012.

[29] J.A. Cunge, F.M. Holly, A. Verwey, Practical Aspects of Computational River Dynamics, Pitman, Boston, USA, 1980.

[30] M.H. Tseng, C.A. Hsu, C.R. Chu, Channel routing in open-channel flows with surges, J. Hydraul. Eng. 127 (2) (2001) 115–122. https://doi.org/10.1061/(ASCE)0733-9429(2001)127:2(115).

[31] H. Capart, T.I. Eldho, S.Y. Huang, D.L. Young, Y. Zech, Treatment of natural geometry in finite volume river flow computations, J. Hydraul. Eng. 129 (5) (2001) 385–393. https://doi.org/10.1061/(ASCE)0733-9429(2003)129:5(385).

[32] M.H. Chaudhry, Open-Channel Flow, second ed., Springer, Berlin, Germany, 2008.

[33] C.V. Bellos, J.G. Sakkas, 1-D dam-break flood-wave propagation on dry bed, J. Hydraul. Eng. 113 (12) (1987) 1510–1524. https://doi.org/10.1061/(ASCE)0733-9429(1987)113:12(1510).

[34] F. Alcrudo, P. Garcia-Navarro, A high-resolution Godunov-type scheme in finite volumes for the 2D shallow-water equations, Int. J. Numer. Meth. Fluids 16 (6) (1993) 489–505. https://10.1002/fld.1650160604.

[35] F. Aureli, A. Maranzoni, P. Mignosa, C. Ziveri, A weighted surface-depth gradient method for the numerical integration of the 2D shallow water equations with topography, Adv. Water Res. 31 (7) (2008) 962–974. https://doi.org/10.1016/j.advwatres.2008.03.005.

[36] Y. Wang, Q. Liang, G. Kesserwani, J.W. Hall, A 2D shallow flow model for practical dam-break simulations, J. Hydraul. Res. 49 (3) (2011) 307–316. https://doi.org/10.1080/00221686.2011.566248.

[37] M. Pilotti, A. Maranzoni, M. Tomirotti, G. Valerio, 1923 Gleno dam break: case study and numerical modeling, J. Hydraul. Eng. 137 (4) (2011) 480–492. https://doi.org/10.1061/(ASCE)HY.1943-7900.0000327.

[38] M. Pilotti, A. Maranzoni, L. Milanesi, M. Tomirotti, G. Valerio, Dam-break modeling in alpine valleys, J. Mt. Sci. 11 (6) (2014) 1429–1441. https://doi.org/10.1007/s11629-014-3042-0.

[39] R. Vacondio, F. Aureli, A. Ferrari, P. Mignosa, A. Dal Palù, Simulation of the January 2014 flood on the Secchia River using a fast and high-resolution 2D parallel shallow-water numerical scheme, Nat. Hazards 80 (1) (2016) 103–125. https://doi.org/10.1007/s11069-015-1959-4.

[40] E.F. Toro, Shock-Capturing Methods for Free-Surface Shallow Flows, John Wiley & Sons, Chichester, UK, 2001.

[41] R.J. LeVeque, Finite Volume Methods for Hyperbolic Problems, Cambridge University Press, Cambridge, UK, 2002.

[42] E.F. Toro, Riemann Solvers and Numerical Methods for Fluid Dynamics: A Practical Introduction, Springer-Verlag, Berlin, Germany, 1997.

[43] A. Maranzoni, P. Mignosa, Seismic-generated unsteady motions in shallow basins and channels. Part I: Smooth analytical solutions, Appl. Math. Model. (submitted) (2018).

[44] A. Balzano, Evaluation of methods for numerical simulation of wetting and drying in shallow water flow models, Coast. Eng. 34 (1–2) (1998) 83–107. https://doi.org/10.1016/S0378-3839(98)00015-5.

[45] M. Antuono, L. Soldini, M. Brocchini, On the role of the Chezy frictional term near the shoreline. Theor. Comp. Fluid Dyn. 26 (1–4) (2012) 105–116. https://doi.org/10.1007/s00162-010-0220-8.

[46] A. Maranzoni, S. Dazzi, F. Aureli, P. Mignosa, Extension and application of the Preissmann slot model to 2D transient mixed flows, Adv. Water Res. 82 (2015) 70–82. https://doi.org/10.1016/j.advwatres.2015.04.010.

[47] J.G. Proakis, D.G. Manolakis, Digital Signal Processing: Principles, Algorithms, and Applications, third ed., Prentice-Hall, Upper Saddle River, New Jersey, USA, 1996.

[48] R.J. Hyndman, A.B. Koehler, Another look at measures of forecast accuracy, Int. J. Forecasting, 22 (4) (2006) 679–688. https://doi.org/10.1016/j.ijforecast.2006.03.001.

[49] B. Bouscasse, M. Antuono, A. Colagrossi, C. Lugni, Numerical and experimental investigation of nonlinear shallow water sloshing, Int. J. Nonlinear Numer. Simul. 14 (2) (2013) 123–138. https://doi.org/10.1515/ijnsns-2012-0100.

[50] ANIDEL, Le Dighe di Ritenuta degli Impianti Idroelettrici Italiani [Dams of Italian Hydropower Plants], Vol. 7, 1953, pp. 223–233 (in Italian).

[51] F. Aureli, P. Mignosa, C. Ziveri, A. Maranzoni, 2D numerical modeling for hydraulic hazard assessment: a

dam-break case study, in: M.S. Altinakar, M.A. Kokpinar, M. Gogus, G. Tayfur, S.Y. Kumcu, N. Yildirim (Eds.), Proceedings of River Flow 2008, Vol. 1, Çeşme, Izmir, Turkey, 2008, pp. 729–736.

[52] F. Aureli, A. Maranzoni, P. Mignosa, A semi-analytical method for predicting the outflow hydrograph due to dam-break in natural valleys, Adv. Water Res. 63 (2014) 38–44. https://doi.org/10.1016/j.advwatres.2013.11.001.

[53] V.T. Chow, Open-Channel Hydraulics, McGraw-Hill, New York, USA, 1959.

[54] L. Luzi, R. Puglia, E. Russo, ORFEUS WG5, Engineering Strong Motion Database, Istituto Nazionale di Geofisica e Vulcanologia, Observatories & Research Facilities for European Seismology, 2016. https://doi.org/10.13127/ESM.

[55] A. Maranzoni, P. Mignosa, Numerical treatment of a discontinuous top surface in 2D shallow water mixed flow modeling, Int. J. Numer. Meth. Fluids 86 (4) (2018) 290–311. https://doi.org/10.1002/fld.4418.

List of figures

Fig. 13. Definition sketch for the problem of sinusoidally-forced sloshing in a parabolic basin.

Fig. 14. Sinusoidally-forced oscillations in a parabolic basin: (a) numerical flow field at $t = 1$ s; (b) slice of analytical and numerical water surfaces along the x-axis for selected times ($h_0 = 0.5$ m, $L = 2.5$ m, $A_x = 0.5g$, $\omega = 2\pi$ rad/s, $D = 10$ s; $\Delta x = \Delta y = 0.02$ m). Only a subset of the numerical points is represented for clarity.

Fig. 15. Sinusoidally-forced oscillations in a parabolic basin: comparison between analytical and numerical time series of water depth and u-velocity component for two selected observation points: (a) $x = 0$, $y = 0$; (b) $x = 2.2$ m, $y = 0$ ($h_0 = 0.5$ m, $L = 2.5$ m, $A_x = 0.5g$, $\omega = 2\pi$ rad/s, $D = 10$ s; $\Delta x = \Delta y = 0.02$ m). Only a subset of the numerical points is represented for clarity.

Fig. 16. Sinusoidally-forced oscillations in a parabolic basin: comparison between analytical and numerical time histories of the shoreline position along the x-axis ($h_0 = 0.5$ m, $L = 2.5$ m, $A_x = 0.5g$, $\omega = 2\pi$ rad/s, $D = 10$ s; $\Delta x = \Delta y = 0.02$ m). Only a subset of the numerical points is represented for clarity.

Fig. 17. Sinusoidally-forced oscillations in a parabolic basin: comparison between analytical and numerical dependences of the dimensionless maximum run-up during the first oscillation on the Strouhal number for $F_x = 2.5$ ($h_0 = 0.5$ m, $L = 2.5$ m, $A_x = 0.5g$; $\Delta x = \Delta y = 0.02$ m).

Fig. 18. S1 sway motion test by Antuono et al. [21]: comparison between experimental and numerical water level variation time series at $x = 0.05$ m (a), $x = 0.10$ m (b), $x = 0.20$ m (c), $x = 0.30$ m (d).

Fig. 19. Bathymetry of the lake created by the Mignano dam.

Fig. 20. Perspective view of the water surface waves induced by a sinusoidal excitation in Lake Mignano, and water surface profiles at Sections A and B indicated in Fig. 19 at selected time $t = 10$ s: forcing acceleration normal to the dam (a, b); forcing acceleration parallel to the dam (c, d). (Amplitude of the forcing acceleration: $0.2g$; excitation period: 1 s; duration of the excitation: 20 s.)

Fig. 21. Numerical time series of water level variation at the dam site for the two excitation scenarios considered (amplitude of the forcing acceleration: $0.2g$; excitation period: 1 s; duration of the excitation: 20 s).

Fig. 22. Numerical modelling of the water waves induced by real seismic excitation in the Mignano reservoir: (a) component accelerogram in the direction normal to the dam; (b) component accelerogram in the direction parallel to the dam; (c) predicted water surface fluctuations at the dam site.

Fig. 23. Plan view of the "Giovanardi" storage tank (water supply system of the town of Parma, Italy). The traces of the beams supporting the ceiling of the tank are reported in dashed lines.

Fig. 24. Example of numerical results obtained for the case study of sinusoidally-forced water waves in the "Giovanardi" storage tank: water depth contour maps and velocity fields at $t = 5$ s for forcing acceleration in the x (a, b) and y (c, d) directions in the case of $h_0 = 2$ m (amplitude of the forcing acceleration: $0.3g$; excitation period: 1 s). Only a subset of the numerical velocity vectors is represented for clarity.

Fig. 25. Numerical piezometric head profiles along selected sections at $t = 3$ s for sinusoidal excitation with $0.3g$ amplitude and 1 s period, in the case of $h_0 = 4$ m: (a) section $y = 4$ m and forcing acceleration in the x-direction; (b) section $x = 27.5$ m and forcing acceleration in the y-direction.

List of tables